23. Riegler, G. R., Garmire, G. P., Moore, W. E. & Stevens, J. A low-energy X-ray polarimeter. *Bull. Am. Phys. Soc.* **15,** 635 (1970).
24. Tsunemi, H. *et al.* Detection of X-ray polarization with a charge coupled device. *Nucl. Instrum. Methods A* **321,** 629–631 (1992).
25. Buschhorn, G. *et al.* X-ray polarimetry using the photoeffect in a CCD detector. *Nucl. Instrum. Methods A* **346,** 578–588 (1994).
26. Soffitta, P. *et al.* Astronomical X-ray polarimetry based on photoelectric effect with microgap detectors. *Nucl. Instrum. Methods A* (in the press); also preprint astro-ph/0012183 at ⟨xxx.lanl.gov⟩ (2000).
27. Angelini, F. *et al.* The micro-gap chamber. *Nucl. Instrum. Methods A* **335,** 69–77 (1993).
28. Austin, R. A., Minamitani, T. & Ramsey, B. Development of a hard X-ray imaging polarimeter. *Proc. SPIE* **2010,** 118–125 (1993).
29. La Monaca, A. *et al.* A new photoelectron imager for X-ray astronomical polarimetry. *Nucl. Instrum. Methods A* **416,** 267–277 (1998).
30. Sauli, F. GEM: a new concept for electron amplification in gas detectors. *Nucl. Instrum. Methods A* **386,** 531–534 (1997).
31. Campbell, M. *et al.* A pixel readout chip for 10–30 Mrad in standard 0.25 μm CMOS. *IEEE Trans. Nucl. Sci.* **46,** 156–160 (1999).
32. Bavdaz, M. *et al.* Status of the X-ray evolving universe spectroscopy mission (XEUS). *Proc. SPIE* **4138,** 69–78 (2000).
33. Christensen, F. E. *et al.* X-ray calibration of the SODART flight telescope. *Proc. SPIE* **3113,** 69–78 (1997).

Acknowledgements

This work is partially supported by the Italian Space Agency (ASI).

Correspondence and requests for materials should be addressed to E.C. (e-mail: costa@ias.rm.cnr.it).

Fabry–Perot interference in a nanotube electron waveguide

Wenjie Liang*†, Marc Bockrath†‡, Dolores Bozovic‡, Jason H. Hafner*, M. Tinkham‡ & Hongkun Park*

** Department of Chemistry and Chemical Biology and ‡ Department of Physics, Harvard University, Cambridge, Massachusetts 02138, USA*
† These authors contributed equally to this work

The behaviour of traditional electronic devices can be understood in terms of the classical diffusive motion of electrons. As the size of a device becomes comparable to the electron coherence length, however, quantum interference between electron waves becomes increasingly important, leading to dramatic changes in device properties[1–8]. This classical-to-quantum transition in device behaviour suggests the possibility for nanometer-sized electronic elements that make use of quantum coherence[1,2,7,8]. Molecular electronic devices are promising candidates for realizing such device elements because the electronic motion in molecules is inherently quantum mechanical[9,10] and it can be modified by well defined chemistry[11–13]. Here we describe an example of a coherent molecular electronic device whose behaviour is explicitly dependent on quantum interference between propagating electron waves—a Fabry–Perot electron resonator based on individual single-walled carbon nanotubes with near-perfect ohmic contacts to electrodes. In these devices, the nanotubes act as coherent electron waveguides[14–16], with the resonant cavity formed between the two nanotube–electrode interfaces. We use a theoretical model based on the multichannel Landauer–Büttiker formalism[17–19] to analyse the device characteristics and find that coupling between the two propagating modes of the nanotubes caused by electron scattering at the nanotube–electrode interfaces is important.

Isolated single-walled nanotubes (SWNTs) were synthesized by chemical vapour deposition[13], and electrical devices based on individual SWNTs were fabricated as reported previously using electron-beam lithography[13]. More than 100 nanotube devices have been made and classified as metallic or semiconducting on the basis of their resistance versus gate voltage (V_g) behaviour[13,20]. Most metallic nanotube devices exhibited room-temperature resistance below 100 kΩ, and more than 20 devices exhibited resistance below 15 kΩ. The lowest resistance values observed in some metallic nanotube devices were around 7 kΩ, approaching the theoretical lower limit of 6.5 kΩ for a nanotube device with perfect ohmic contacts[2,14,21]. This observation indicates that the contacts between nanotubes and the Au/Cr electrodes in our nanotube devices are nearly perfect, unlike those in previous SWNT devices[13,16,21–24], and that electrons can pass through the nanotube–metal junction with little reflection. The following discussion concentrates on metallic nanotube devices with room-temperature resistances below 15 kΩ.

Figure 1 shows a differential conductance ($\partial I/\partial V$)–V_g plot near zero bias ($V = 0$) obtained from a representative nanotube device at a temperature $T = 4$ K. The length of the nanotube segment (L) between two electrodes was around 200 nm, as determined by atomic force microscopy. Below $T = 10$ K, the device exhibits pronounced $\partial I/\partial V$ oscillations that are quasi-periodic in V_g with an average conductance of around $3.2\,e^2/h$ (the value of e^2/h is 38.8 μS or $(25.8\,\mathrm{k\Omega})^{-1}$). Figure 2 shows two-dimensional $\partial I/\partial V$ plots as a function of V and V_g obtained from nanotube devices with $L \approx 530$ nm and $L \approx 220$ nm, respectively. The dips in $\partial I/\partial V$ appear as dark lines in Fig. 2. The positions of the $\partial I/\partial V$ dips evolve smoothly as V and V_g change, forming a mesh of crisscrossing dark lines. Similar $\partial I/\partial V$–V–V_g patterns were observed in 10 other devices with average conductance above $2e^2/h$, although the V and V_g spacing between adjacent dark lines changed from device to device. The conductance behaviour of these devices did not change substantially as the temperature was reduced from 4 K to 100 mK.

Figures 1 and 2 illustrate several characteristics shared by all 12 nanotube devices that exhibit $\partial I/\partial V$ oscillations. The average values of $\partial I/\partial V$ were around $2–3\,e^2/h$, and $\partial I/\partial V$ remained above e^2/h irrespective of V, V_g and T, clearly indicating that the electrical behaviour of these nanotube devices is distinct from those reported

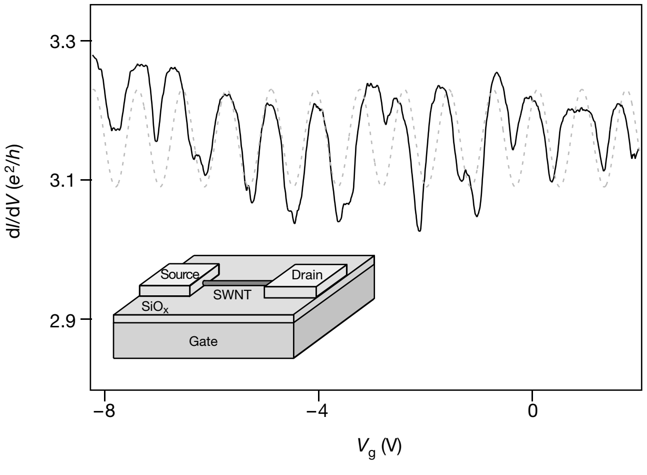

Figure 1 Zero-bias differential conductance ($\partial I/\partial V$) of a 200-nm SWNT device plotted against gate voltage (V_g). Isolated SWNTs were synthesized on a degenerately doped silicon wafer with a 1-μm oxide layer by chemical vapour deposition. Individual SWNTs with ~1-nm height were located by atomic force microscopy, and nanotube devices were fabricated by defining two Au/Cr electrodes on top of the SWNTs by electron-beam lithography. Electrical properties of nanotube devices were characterized as a function of bias voltage (V) and V_g. The degenerately doped silicon substrate was used as a gate electrode to modulate the charge density and the Fermi-level position within the nanotubes. The dotted curve shows a sinusoidal function with the same average period as the measured data. Comparison between these two plots shows that the measured data is quasi-periodic in V_g. Inset, a schematic diagram of the SWNT device, showing a nanotube with attached leads, the insulating gate oxide and the degenerately doped silicon gate.

previously that exhibited a Coulomb-blockade behaviour[13,16,21–25]. In addition, the $\partial I/\partial V$ dips were typically more pronounced than $\partial I/\partial V$ peaks, as shown by the dominant dark lines in Fig. 2. Most importantly, the V and V_g spacing between adjacent dark lines increased as L decreased. This last behaviour is best quantified by the bias voltage (V_c) at the crossing point between adjacent left- and right-sloped dark lines: inspection of Fig. 2 shows that V_c for the 530-nm device is around 3.5 mV, whereas V_c for the 220-nm device is around 6.5 mV. The inset in Fig. 2 shows the plot of V_c against L^{-1} obtained from seven different devices where V_c can be unambiguously determined, and it clearly shows the linear relationship between V_c and L^{-1}.

Previous experimental[15,21–28] and theoretical[14,21] studies have indicated that metallic SWNTs behave as a one-dimensional ballistic conductor where the current is carried by two spin-degenerate one-dimensional transport modes with linear dispersion (Fig. 3). The maximum $\partial I/\partial V$ value near zero bias expected for a SWNT device is therefore $4e^2/h$, obtained only when electrons pass through the nanotube–metal interfaces without reflection[2,14]. The mean conductance values in Figs 1 and 2 are smaller than this theoretical maximum, indicating electron scattering in the nanotube devices. The linear relationship between V_c and L^{-1} in Fig. 2 (inset) provides experimental evidence that the electron scattering occurs mostly at the nanotube–metal interface and that electrons pass through the nanotube ballistically.

This picture of interfacial electron scattering coupled with ballistic electron transport within the nanotube indicates that the nanotube-device characteristics may be determined by quantum interference between electron waves multiply reflected between two nanotube–metal interfaces, analogous to the light transmission in an optical Fabry–Perot cavity[29]. Figures 1 and 2 show that $\partial I/\partial V$ oscillates as a function of V_g and V, and the oscillation period exhibits an inverse dependence on the nanotube length. Because V_g modulates the Fermi-level position in the nanotube and hence changes the Fermi wave number (2π/wavelength) k for electrons, the observed $\partial I/\partial V$ oscillations can be attributed to the change in k, just as in the case of transmitted intensity oscillations in an optical cavity.

The observed electron-wave interference can be understood quantitatively on the basis of a theoretical model shown schematically in Fig. 3. In this model, which is based on the multichannel Landauer–Büttiker formalism[2,17–19], the nanotube is considered as a coherent electron waveguide with two propagating modes, and the electron scattering is modelled by 4 × 4 scattering (S) matrices at each interface, $\mathbf{S_L}$ and $\mathbf{S_R}$. Following previous theoretical studies[14,21], the electron scattering between the two modes inside the nanotube is ignored, and the phase accumulation during electron propagation is represented by a diagonal 4 × 4 matrix $\mathbf{S_N}$. Inter-mode coupling can still occur through the electron scattering at the interfaces, and the matrix elements of $\mathbf{S_L}$ and $\mathbf{S_R}$ represent not only the electron transmission and reflection within the same modes but also the coupling between the two propagation modes.

One important difference between the nanotube electron cavity and a simple single-mode optical cavity arises from the fact that the two propagating modes in SWNTs are characterized by different wave vectors, $\vec{k}_1$ and $\vec{k}_2$ (refs 14, 21). In an isolated neutral SWNT, $\vec{k}_1$ and $\vec{k}_2$ are the same and they are both given by $\vec{k}_0$ ($k_0 = 8.44\,\mathrm{nm}^{-1}$). In our nanotube devices, however, $\vec{k}_1$ and $\vec{k}_2$ are in general different owing to the linear band dispersion in SWNTs, and the difference between $\vec{k}_1$ and $\vec{k}_2$ grows linearly as the Fermi level is shifted by V_g. Consequently, electrons in the two propagating modes acquire different phase shifts as they traverse the nanotube, which are represented by the diagonal matrix elements of $\mathbf{S_N}$. The phase change as a function of electron energy is responsible for the interference patterns as a function of V and V_g in Figs 1 and 2.

The calculation of the $\partial I/\partial V$ patterns requires knowledge of the matrix elements of $\mathbf{S_L}$ and $\mathbf{S_R}$, each containing 16 independent parameters in general. To reduce the number of parameters in the theoretical fit to the experimental data, most calculations were performed in the reduced parameter space. Specifically, both $\mathbf{S_L}$ and $\mathbf{S_R}$ were defined by exponentiating a hermitian matrix that contains just four parameters, r_1, r_2, δ_1 and δ_2 (see Methods). The resulting S matrices exhibit the required unitarity and properties

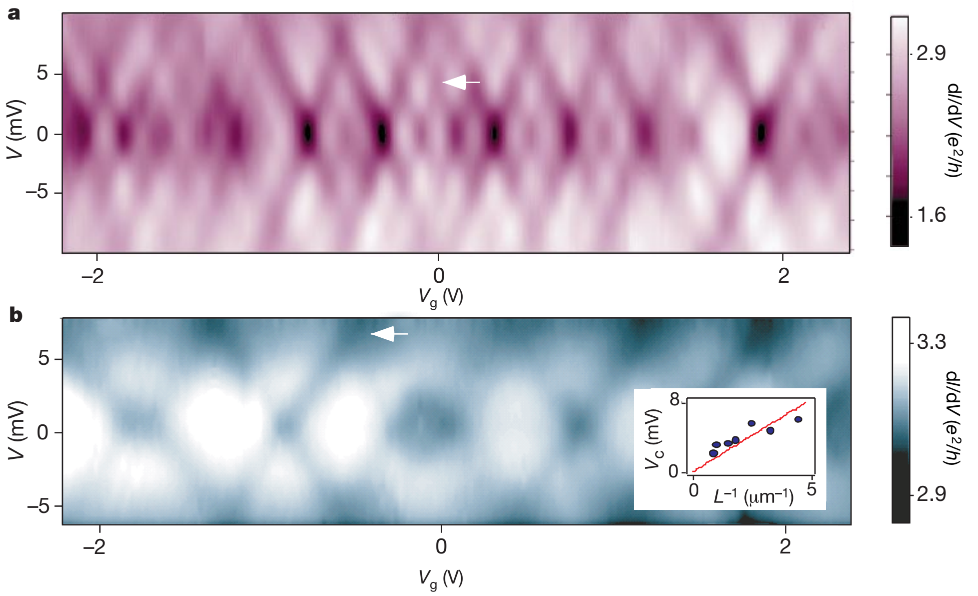

Figure 2 Two-dimensional $\partial I/\partial V$ plots as a function of V and V_g measured at $T = 4$ K. **a**, Data from a 530-nm SWNT device; **b**, data from a 220-nm SWNT device. Both plots show a quasi-periodic pattern of crisscrossing dark lines that correspond to the $\partial I/\partial V$ dips as V and V_g are varied. The bias voltage values (V_c) at which adjacent positively and negatively sloped lines intersect (white arrows) quantify the energy scales for $\partial I/\partial V$ oscillations. In **a**, V_c is ~3.5 meV; in **b**, V_c is ~6.5 meV. Inset, values of V_c from seven devices plotted against the inverse nanotube length (L^{-1}). The solid curve is a line with a slope equal to $hv_F/2 = 1{,}670\,\mathrm{meV\,nm^{-1}}$, where $v_F = 8.1 \times 10^5\,\mathrm{m\,s^{-1}}$ is the Fermi velocity in the nanotube.

demanded by time-reversal symmetry. Here r_1 and r_2 correspond to (up to a constant) the magnitude of the electron reflection matrix elements in the first-order Born approximation with and without the inter-mode hopping, while δ_1 and δ_2 signify the phases of these matrix elements[19].

The calculations were further simplified by assuming that $\mathbf{S_L}$ and $\mathbf{S_R}$ are mirror images of each other. This assumption is motivated by the experimental observation that the $V - V_g$ slopes of right- and left-sloping $\partial I/\partial V$ lines are nearly identical and thus the electron reflection probabilities at the two interfaces are approximately the same in most devices[30]. $\mathbf{S_L}$ and $\mathbf{S_R}$ were also assumed to be energy independent over the energy range accessed in the experiment. With these approximations, the theoretical fit to the experimental data can be performed using four parameters.

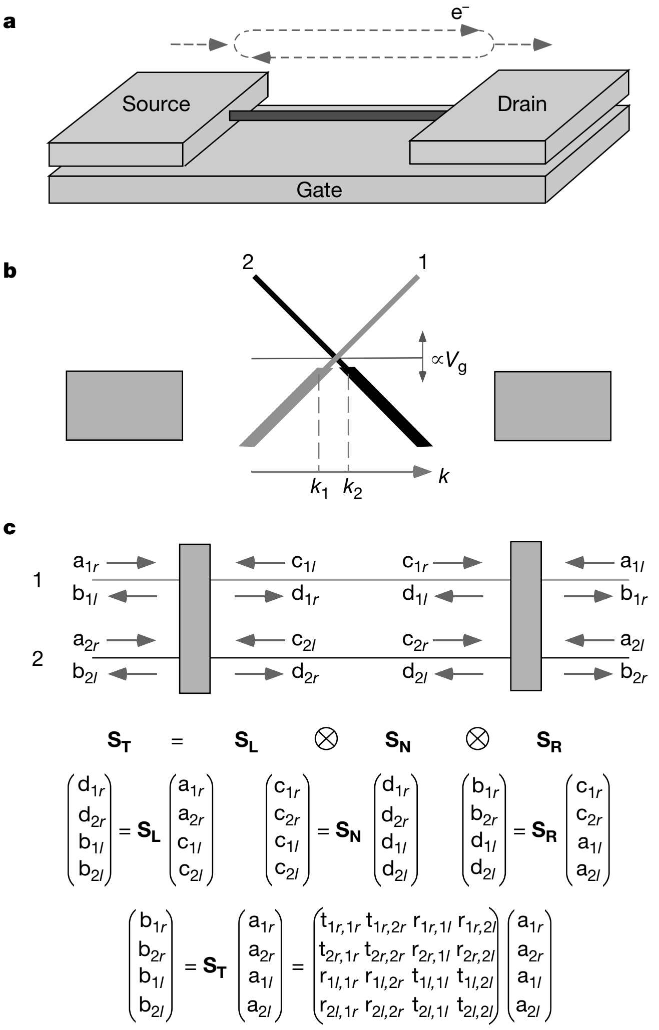
a
e⁻
Source
Drain
Gate
b
2
1
$\propto V_g$
k_1 k_2
k
c
1
2
a_{1r} b_{1l} c_{1l} d_{1r} c_{1r} d_{1l} a_{1l} b_{1r}
a_{2r} b_{2l} c_{2l} d_{2r} c_{2r} d_{2l} a_{2l} b_{2r}
$\mathbf{S_T} = \mathbf{S_L} \otimes \mathbf{S_N} \otimes \mathbf{S_R}$
$\begin{pmatrix} d_{1r}\\ d_{2r}\\ b_{1l}\\ b_{2l}\end{pmatrix} = \mathbf{S_L}\begin{pmatrix} a_{1r}\\ a_{2r}\\ c_{1l}\\ c_{2l}\end{pmatrix}$
$\begin{pmatrix} c_{1r}\\ c_{2r}\\ c_{1l}\\ c_{2l}\end{pmatrix} = \mathbf{S_N}\begin{pmatrix} d_{1r}\\ d_{2r}\\ d_{1l}\\ d_{2l}\end{pmatrix}$
$\begin{pmatrix} b_{1r}\\ b_{2r}\\ d_{1l}\\ d_{2l}\end{pmatrix} = \mathbf{S_R}\begin{pmatrix} c_{1r}\\ c_{2r}\\ a_{1l}\\ a_{2l}\end{pmatrix}$
$\begin{pmatrix} b_{1r}\\ b_{2r}\\ b_{1l}\\ b_{2l}\end{pmatrix} = \mathbf{S_T}\begin{pmatrix} a_{1r}\\ a_{2r}\\ a_{1l}\\ a_{2l}\end{pmatrix} = \begin{pmatrix} t_{1r,1r} & t_{1r,2r} & r_{1r,1l} & r_{1r,2l}\\ t_{2r,1r} & t_{2r,2r} & r_{2r,1l} & r_{2r,2l}\\ r_{1l,1r} & r_{1l,2r} & t_{1l,1l} & t_{1l,2l}\\ r_{2l,1r} & r_{2l,2r} & t_{2l,1l} & t_{2l,2l}\end{pmatrix}\begin{pmatrix} a_{1r}\\ a_{2r}\\ a_{1l}\\ a_{2l}\end{pmatrix}$

Figure 3 A theoretical model that explains the observed interference patterns. **a**, Schematic diagram of a SWNT device illustrating the multiple electron reflection that gives rise to the observed interference pattern. **b**, Diagram of the band dispersion relation of a metallic SWNT near a band-crossing point. In SWNTs, electronic states near two Fermi points located at $\vec{\mathbf{K}} = \vec{k}_0$ and $\vec{\mathbf{K}}' = -\vec{k}_0$ contribute to the electrical conduction. The diagram shown here depicts only the band dispersion relation near $\vec{\mathbf{K}}$ for clarity. At the $\vec{\mathbf{K}}$ ($\vec{\mathbf{K}}'$) point, two bands derived from the bonding (π) and antibonding (π^*) orbitals between neighbouring carbon atoms cross with equal slopes of opposite sign. The thick lines represent the electron filling in each band. The diagram shows the effect of V_g on the electron filling in SWNTs when V is zero. The shift of the band edge (or the band-crossing point) with V_g results in a change in the charge density in the nanotube, which, in turn, changes the Fermi wave numbers k_1 and k_2. **c**, A diagram illustrating the basis wave functions used for defining the S-matrices $\mathbf{S_L}$, $\mathbf{S_N}$, $\mathbf{S_R}$ and $\mathbf{S_T}$. The basis-set ordering was chosen so that the total scattering matrix $\mathbf{S_T}$ is a unit diagonal matrix in the absence of interfacial scattering.

The overall conductance behaviour of a nanotube device can be calculated once the device S matrix $\mathbf{S_T}$ is obtained from $\mathbf{S_L}$, $\mathbf{S_R}$ and $\mathbf{S_N}$ by matrix combination[2,17–19]. Specifically, in the zero-temperature limit, $\partial I/\partial V$ as a function of V and V_g in a nanotube device is related to the matrix elements of $\mathbf{S_T}$ as (see Methods for derivation)

$$\frac{\partial I}{\partial V}(V, V_g) = \frac{2e^2}{h}\left[\sum_{i,j=1,2}\left|t_{il,jr}\left(\frac{eV}{2\hbar v_F} + \frac{\pi}{4}\frac{C_L V_g}{e}\right)\right|^2 + \sum_{i,j=1,2}\left|t_{il,jr}\left(\frac{-eV}{2\hbar v_F} + \frac{\pi}{4}\frac{C_L V_g}{e}\right)\right|^2\right]$$

In this formula, $t_{il,jr}$ represents matrix elements of $\mathbf{S_T}$ defined in Fig. 3, v_F is the Fermi velocity inside the nanotube ($v_F \approx 8 \times 10^5\ \mathrm{m\,s^{-1}}$), and C_L is the capacitance per unit length of a nanotube. This formula specifies not only the linear-response behaviour of a nanotube device but also its nonlinear response upon the application of the bias voltage. Although the above formula is derived for the zero-temperature limit, it can still be used to fit the data in Fig. 2 because the observed conductance behaviour did not change as the temperature was lowered from 4 K to 100 mK and hence thermal smearing had little role in determining the transport properties.

The result of the theoretical fit for the 220-nm nanotube device is presented in Fig. 4 along with the experimental data. The theoretical fit clearly accounts for the major features in the data satisfactorily. Although they are not shown, the calculations reproduced experimental data from other devices as well. One of the most important successes of the model is that it explains the energy scale of the observed $\partial I/\partial V$ oscillations (represented by eV_c) without any adjustable parameters. As shown in Fig. 3, two bands in SWNTs have E–k slopes with equal magnitude and opposite sign. This band structure guarantees that whenever the Fermi-level change causes the additional round-trip phase shift of $+2\pi$ in one mode, the other mode acquires a phase shift of -2π. The value of V_c can therefore be obtained by setting the round trip phase shift $2LeV_c/(\hbar v_F)$ equal to 2π. Figure 2 (inset) shows a red line obtained from this expression along with experimental data. It shows that the theoretical model explains experimental V_c values very well without any adjustable parameters.

Figure 4 also shows that the theoretical model can explain the predominance of $\partial I/\partial V$ dips over the peaks in the data. Inspection of the fitting parameters, r_1, r_2, δ_1 and δ_2, shows that the pronounced $\partial I/\partial V$ dips cannot be reproduced without the inter-mode coupling at the interface (represented by r_1 in our fit), especially when the average conductance of the device is above $3e^2/h$ as in Fig. 4. This observation strongly suggests that the inter-mode coupling at the nanotube–metal interface is important in our device geometry. To test whether this conclusion is dependent on the number of fitting parameters, a more extensive model fit was performed, with $\mathbf{S_L}$ and $\mathbf{S_R}$ containing more than four parameters. The results confirm that the inter-mode coupling is indeed required to explain the dominance of $\partial I/\partial V$ dips.

Despite the good agreement between theory and experiment shown in Fig. 4, several features in the experimental data remain unexplained by the theoretical model. Most notably, Fig. 1 shows that the magnitudes of the observed $\partial I/\partial V$ dips are not uniform and show variations on the order of $0.1e^2/h$ as V_g is varied. Moreover, Fig. 2a shows that this variation leads to superstructures in the two-dimensional plot that are not periodic in V_g. These observations may indicate the possible effects of disorder on electron propagation in the nanotube. This disorder is likely to arise from the underlying substrate or at the interface because intrinsic nanotube defects change electron transport properties much more markedly[13]. Figure 2 also shows that the magnitudes of $\partial I/\partial V$ modulation

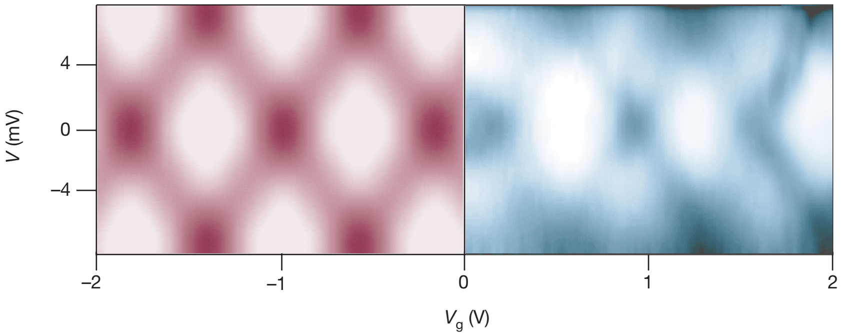

Figure 4 The calculated (left, shown in red) and measured (right, shown in blue) two-dimensional $\partial I/\partial V$ plots as a function of V and V_g for a 220-nm SWNT device. These plots have been shifted in V_g for easy comparison. In both plots, dark corresponds to $2.9\,e^2/h$, and white corresponds to $3.2\,e^2/h$. The theoretical calculation was performed by setting $r_1 = 0.2$, $r_2 = 0.25$, $\delta_1 = 0.4$, $\delta_2 = 0.95$ for both $\mathbf{S_L}$ and $\mathbf{S_R}$ and with $C_L \approx$ 20 electrons V^{-1} μm^{-1} (V in V_g).

diminish as $|V|$ is increased. This observation suggests the occurrence of heating or dephasing when the electron energy distribution deviates from equilibrium. The dephasing may arise from the fact that the nanotube–metal interface is not abrupt and instead spans many atoms. ☐

Methods

The explicit forms of $\mathbf{S_L}$, $\mathbf{S_R}$ and $\mathbf{S_N}$

The S matrices, $\mathbf{S_L}$, $\mathbf{S_R}$ and $\mathbf{S_N}$, and the basis wave functions are defined in Fig. 3. Assuming that the electron scattering between the two modes inside the nanotube is ignored[14,21], the matrix $\mathbf{S_N}$ is given by

$$\mathbf{S_N} = \begin{bmatrix} e^{i\phi_1} & 0 & 0 & 0 \\ 0 & e^{i\phi_2} & 0 & 0 \\ 0 & 0 & e^{i\phi_1} & 0 \\ 0 & 0 & 0 & e^{i\phi_2} \end{bmatrix} \tag{1}$$

Here ϕ_1 and ϕ_2 are the phases accumulated by electrons in the two transport modes upon traversing the nanotube segment between the metal electrodes. In general, $\mathbf{S_L}$ and $\mathbf{S_R}$ each contain 16 independent parameters. To reduce the number of parameters in the theoretical fit of experimental data, $\mathbf{S_L}$ and $\mathbf{S_R}$ were parameterized on the basis of the first-order Born approximation. Assuming a weak scattering potential Δ at the interface, the scattering matrices at the interface can be obtained using the Born approximation[19]

$$S_{mn} \approx \delta_{mn} + ia_{mn} = \delta_{mn} + \frac{i}{\hbar v_F}\langle\psi_m|\Delta|\psi_n\rangle \tag{2}$$

Here δ_{mn} is the Kronecker delta, and ψ_m represents mode wave functions defined in Fig. 3. Note that the S matrix in equation (2) is only unitary to first order in Δ. To make it unitary, the S matrix was taken to be the matrix exponential of $\{a_{nm}\}$ $S = \exp(i\mathbf{a})$. Specifically, the calculation shown in Fig. 4 was performed using the following ansatz for $\mathbf{S_R}$ and $\mathbf{S_L}$:

$$\mathbf{S_{R(L)}} = \exp\left(i \begin{bmatrix} 0 & 0 & r_2 & r_1\exp(\pm i\delta_1) \\ 0 & 0 & r_1\exp(\pm i\delta_1) & r_2\exp(\pm i\delta_2) \\ r_2 & r_1\exp(\mp i\delta_1) & 0 & 0 \\ r_1\exp(\mp i\delta_1) & r_2\exp(\mp i\delta_2) & 0 & 0 \end{bmatrix} \right) \tag{3}$$

Here r_1 and r_2 are proportional to the magnitude of the electron reflection matrix elements in the first-order Born approximation with and without the inter-mode hopping, respectively, and δ_1 and δ_2 signify the phases of these matrix elements. As described in the text, the definitions of $\mathbf{S_R}$ and $\mathbf{S_L}$ in equation (3) ensure the opposite parity between the left and right electrodes relative to the nanotube. The scattering matrices $\mathbf{S_R}$ and $\mathbf{S_L}$ are further assumed to be independent of energy. Therefore, the conductance variation as a function of V and V_g depends only on the phase shifts $\phi_{1,2}$ that appear in $\mathbf{S_N}$.

Derivation of the expression for $\partial I/\partial V$

A non-zero source-drain bias V raises the electrochemical potential of the left electrode by $eV/2$ and lowers the electrochemical potential of the right electrode by $eV/2$. Because the electron transport through the nanotube is ballistic, the total energy of the electrons involved in transport is conserved. The total energy $E(-eV/2 < E < eV/2)$ of electrons at the Fermi surface can be expressed as a sum of their kinetic energy $K(x)$ and the local self-consistent potential energy $\Phi_{eV}(x)$, where x is the spatial position along the nanotube:

$$K(x) + \Phi_{eV}(x) = E \tag{4}$$

The wave numbers $k_{1,2}$ of the electrons in the two transport modes are given by

$$k_{1,2}(x) = k_0 \pm \frac{K(x)}{\hbar v_F} = k_0 \pm \frac{E - \Phi_{eV}(x)}{\hbar v_F} \tag{5}$$

and the resulting phase shifts are given by

$$\phi_{1,2} = \int_0^L k_{1,2}(x)\mathrm{d}x = \int_0^L \left(k_0 \pm \frac{E - \Phi_{eV}(x)}{\hbar v_F}\right)\mathrm{d}x = k_0 L \pm \frac{E - \langle\Phi_{eV}\rangle}{\hbar v_F} L \tag{6}$$

Here $\langle\Phi_{eV}\rangle$ is the value of the self-consistent potential averaged over the nanotube length L. $\langle\Phi_{eV}\rangle$ can be related to the excess charge Q on the nanotube using the local density of states per unit length $\rho(0) = 8/(hv_F)$ at the Fermi level:

$$Q = -\int_0^L e\Phi_{eV}(x)\rho(0)\mathrm{d}x = -\frac{8Le}{hv_F}\langle\Phi_{eV}\rangle \tag{7}$$

From equations (6) and (7), it follows that

$$\phi_{1,2} = k_0 L \pm \frac{E}{\hbar v_F} L \pm \frac{\pi}{4}\frac{Q}{e} \tag{8}$$

As $\mathbf{S_L}$ and $\mathbf{S_R}$ are mirror images of each other, the total charge on the nanotube Q is unaffected by V. Therefore, Q can be related to V_g by $Q = LC_L V_g$, where C_L is the capacitance per unit length. The result for $\phi_{1,2}$ can thus be obtained as

$$\phi_{1,2} = k_0 L \pm \left(\frac{E}{\hbar v_F} L + \frac{\pi}{4}\frac{LC_L V_g}{e}\right) \tag{9}$$

The phases, $\phi_{1,2}$, given by equation (9) determine $\mathbf{S_N}$. The matrix $\mathbf{S_T}$ can be obtained by combining $\mathbf{S_L}$, $\mathbf{S_R}$ and $\mathbf{S_N}$ by matrix combination[2,17–19]. Once $\mathbf{S_T}$ is known, the current through the nanotube can be calculated by

$$I = \frac{2e}{h}\int_{-eV/2}^{eV/2} \mathrm{d}E \sum_{i,j=1,2} \left| t_{il,jr}\left(\frac{E}{\hbar v_F} + \frac{\pi}{4}\frac{C_L V_g}{e}\right)\right|^2 \tag{10}$$

where the matrix elements $t_{il,jr}$ are defined in Fig. 3. The differentiation of equation (10) leads to the expression for $\partial I/\partial V$ given in the text.

Received 29 December 2000; accepted 14 March 2001.

1. Ando, T. *et al. Mesoscopic Physics and Electronics* (Springer, Berlin, 1998).
2. Datta, S. *Electronic Transport in Mesoscopic Systems* (Cambridge Univ. Press, Cambridge, 1995).
3. van Wees, B. J. *et al.* Observation of zero-dimensional states in a one-dimensional electron interferometer. *Phys. Rev. Lett.* **62,** 2523–2526 (1989).
4. Crommie, M., Lutz, C. P. & Eigler, D. M. Confinement of electrons to quantum corrals on a metal surface. *Science* **262,** 218–220 (1993).
5. Ji, Y. *et al.* Phase evolution in a Kondo-correlated system. *Science* **290,** 779–783 (2000).
6. Topinka, M. A. *et al.* Imaging coherent electron flow from a quantum point contact. *Science* **289,** 2323–2326 (2000).
7. Manoharan, H. C., Lutz, C. P. & Eigler, D. M. Quantum mirages formed by coherent projection of electronic structure. *Nature* **403,** 512–515 (2000).
8. Debray, P. *et al.* Ballistic electron transport in stubbed quantum waveguides: Experiment and theory. *Phys. Rev. B* **61,** 10950–10958 (2000).
9. Joachim, C., Gimzewski, J. K. & Aviram, A. Electronics using hybrid-molecular and mono-molecular devices. *Nature* **408,** 541–548 (2000).
10. Park, H. *et al.* Nano-mechanical oscillations in a single-C$_{60}$ transistor. *Nature* **407,** 57–60 (2000).
11. Chen, J., Reed, M. A., Rawlett, A. M. & Tour, J. M. Large on-off ratios and negative differential resistance in a molecular electronic device. *Nature* **286,** 1550–1552 (1999).
12. Collier, C. P. *et al.* A [2]catenane-based solid state electronically reconfigurable switch. *Science* **289,** 1172–1175 (2000).

13. Bockrath, M. *et al.* Resonant electron scattering by defects in single-walled carbon nanotubes. *Science* **291,** 283–285 (2001).
14. White, C. T. & Todorov, T. N. Carbon nanotubes as long ballistic conductors. *Nature* **393,** 240–242 (1998).
15. Frank, S., Poncharal, P., Wang, Z. L. & De Heer, W. A. Carbon nanotube quantum resistors. *Science* **280,** 1744–1746 (1998).
16. Dekker, C. Carbon nanotubes as molecular quantum wires. *Phys. Today* **52 (5),** 22–28 (1999).
17. Büttiker, M., Imry, Y., Landauer, R. & Pinhas, S. Generalized many-channel conductance formula with application to small rings. *Phys. Rev. B* **31,** 6207–6215 (1985).
18. Büttiker, M. Role of quantum coherence in series resistors. *Phys. Rev. B* **33,** 3020–3026 (1986).
19. Cahay, M., McLennan, M. & Datta, S. Conductance of an array of elastic scatterers: A scattering-matrix approach. *Phys. Rev. B* **37,** 10125–10136 (1988).
20. Tans, S. J., Verschueren, A. R. M. & Dekker, C. Room-temperature transistor based on a single carbon nanotube. *Nature* **393,** 49–52 (1998).
21. McEuen, P. L. *et al.* Disorder, pseudospins, and backscattering in carbon nanotubes. *Phys. Rev. Lett.* **83,** 5098–5101 (1999).
22. Bockrath, M. *et al.* Single-electron transport in ropes of carbon nanotubes. *Science* **275,** 1922–1925 (1997).
23. Tans, S. J. *et al.* Individual single-wall carbon nanotubes as quantum wires. *Nature* **386,** 474–476 (1997).
24. Tans, S. J., Devoret, M. H., Groeneveld, R. J. A. & Dekker, C. Electron–electron correlations in carbon nanotubes. *Nature* **394,** 761–764 (1998).
25. Nygard, J., Cobden, D. H. & Lindelof, P. E. Kondo physics in carbon nanotubes. *Nature* **408,** 342–346 (2000).
26. Venema, L. C. *et al.* Imaging electron wave functions of quantized energy levels in carbon nanotubes. *Science* **283,** 52–55 (1999).
27. Bachtold, A. *et al.* Aharonov-Bohm oscillations in carbon nanotubes. *Nature* **397,** 673–675 (1999).
28. Tsukagoshi, K., Alphenaar, B. W. & Ago, H. Coherent transport of electron spin in a ferromagnetically contacted carbon nanotube. *Nature* **401,** 572–574 (1999).
29. Hecht, E. *Optics* (Addison-Wesley, Reading, 1987).
30. Sohn, L. L., Kouwenhoven, L. P. & Schön, G. *Mesoscopic Electron Transport* (Kluwer, Dordrecht, 1997).

Acknowledgements

We thank C. M. Lieber for providing facilities to synthesize SWNTs; and C. M. Lieber, B. I. Halperin, E. J. Heller and C. Marcus for discussions and advice. This work is supported by NSF and ONR (M.T.) and the Dreyfus Foundation, NSF, and Harvard University (H.P.). J.H.H. was supported by NIH.

Correspondence and requests for materials should be addressed to H.P.
(e-mail: HPark@chemistry.harvard.edu).

Non-Fermi-liquid behaviour in $La_4Ru_6O_{19}$

P. Khalifah*, K. D. Nelson†, R. Jin†, Z. Q. Mao†, Y. Liu†, Q. Huang‡, X. P. A. Gao§, A. P. Ramirez§¶ & R. J. Cava*

* *Department of Chemistry and Princeton Materials Institute, Princeton University, Princeton, New Jersey 08540, USA*
† *Department of Physics, The Pennsylvania State University, University Park, Pennsylvania 16802, USA*
‡ *NIST Center for Neutron Research, National Institute of Standards and Technology, Gaithersburg, Maryland 20899; and Department of Materials and Nuclear Engineering, University of Maryland, College Park, Maryland 20742, USA*
§ *Lucent Technologies, Murray Hill, New Jersey 07974, USA*

Understanding the complexities of electronic and magnetic ground states in solids is one of the main goals of solid-state physics. Transition-metal oxides have proved to be particularly fruitful in this regard, especially for those materials with the perovskite structure, where the special characteristics of transition-metal–oxygen orbital hybridization determine their properties. Ruthenates have recently emerged as an important family of perovskites because of the unexpected evolution from high-temperature ferromagnetism in $SrRuO_3$ to low-temperature superconductivity in Sr_2RuO_4 (refs 1, 2). Here we show that a ruthenate in a different structural family, $La_4Ru_6O_{19}$, displays a number of highly unusual properties, most notably non-Fermi-liquid behaviour. The properties of $La_4Ru_6O_{19}$ have no analogy among the thousands of previously characterized transition-metal oxides. Instead, they resemble those of $CeCu_{6-x}Au_x$—a widely studied *f*-electron-based heavy fermion intermetallic compound that is often considered as providing the best example of non-Fermi-liquid behaviour. In the ruthenate, non-Fermi-liquid behaviour appears to arise from just the right balance between the interactions of localized electronic states derived from Ru–Ru bonding and delocalized states derived from Ru–O hybridization.

The unusual properties of $La_4Ru_6O_{19}$ are accentuated by comparison to the highly related compound $La_3Ru_3O_{11}$. Both have cubic crystal structures[3,4] that are a derivative of the $KSbO_3$ structure type. The structures (Fig 1a and b) contain pairs of edge-shared RuO_6 octahedra, effectively forming Ru_2O_{10} dimers, which are connected to other dimers through corner-shared oxygens. The result is a fully three-dimensional ruthenium–oxygen network that has the same geometry for both compounds. The formal ruthenium oxidation state is +4.33 in both compounds, leading to the same number of available electrons to fill the electronic states in the Ru–O network. Direct metal–metal bonding occurs in $La_4Ru_6O_{19}$, where the Ru–Ru distance within the dimers, 2.49 Å, is unusually short[3]. No Ru–Ru bonding occurs in $La_3Ru_3O_{11}$ (ref. 4). The presence of distinct metal–metal bonded dimers in $La_4Ru_6O_{19}$ should lead to the existence of localized electronic states in addition to the many delocalized states usually seen in ruthenates due to the strong Ru–O orbital hybridization[5,6]. This leads to a profound difference in the electronic properties of the two compounds.

Single crystals of $La_4Ru_6O_{19}$ and $La_3Ru_3O_{11}$ were grown by placing 0.2 g of dried La_2O_3 and RuO_2 mixed in the stoichiometric ratios, 1 g of KCl and 0.131 g of $KClO_3$ in a 2-ml Al_2O_3 crucible. The crucible was sealed in an evacuated quartz tube, and heated at 900 °C for three to four days. The single crystals (up to 0.3 mm in dimension) were removed from the flux and cleaned by washing with distilled water. The large (15 g) polycrystalline powder sample of $La_4Ru_6O_{19}$ that we used in the neutron-diffraction experiments was synthesized in an analogous manner, but without KCl.

The temperature-dependent resistivity for a representative single crystal of $La_4Ru_6O_{19}$ is presented in Fig. 2, as is the normalized resistance of a representative $La_3Ru_3O_{11}$ crystal. A room-temperature resistivity of 2.5 mΩ cm was observed for $La_4Ru_6O_{19}$, slightly lower than the value previously reported for polycrystalline material[7]. This resistivity is significantly larger than the

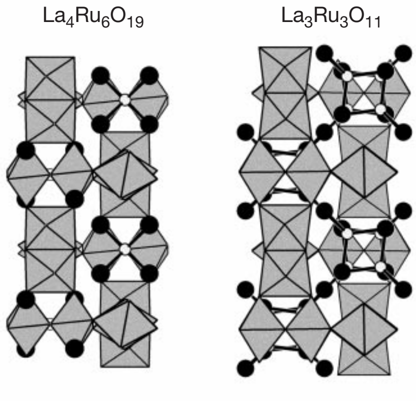

Figure 1 Two crystallographic unit cells of $La_4Ru_6O_{19}$ nd $La_3Ru_3O_{11}$. RuO_6 octahedra are shown as shaded polyhedra (with Ru atoms inside). The virtually identical Ru–O network is seen for each. La and non-network O atoms are shown by filled and open circles, respectively.

[¶] Present address: Condensed Matter and Thermal Physics Group, Los Alamos National Laboratory, Los Alamos, New Mexico 87545, USA.